JGR Space Physics

RESEARCH ARTICLE
10.1029/2024JA032414

Key Points:

- With a new inversion scheme we resolve the full current based on ground and space magnetometers and spherical elementary current systems
- During substorms and close to the onset the ground-based equivalent field-aligned current is a poor proxy for the field-aligned current
- The intensification of the westward electrojet can be a false indication of the formation of the substorm current wedge

Correspondence to:
S. J. Walker,
walker@cp.dias.ie

Citation:
Walker, S. J., Laundal, K. M., Reistad, J. P., Hatch, S. M., Ohma, A., & Gjerloev, J. (2024). The ionospheric leg of the substorm current wedge: Combining iridium and ground magnetometers. *Journal of Geophysical Research: Space Physics*, *129*, e2024JA032414. https://doi.org/10.1029/2024JA032414

Received 3 JAN 2024
Accepted 21 JUN 2024

Author Contributions:
Conceptualization: Simon James Walker
Formal analysis: Simon James Walker
Investigation: Simon James Walker, Karl Magnus Laundal, Jone Peter Reistad, Spencer Mark Hatch, Anders Ohma
Methodology: Simon James Walker
Software: Simon James Walker
Supervision: Karl Magnus Laundal, Jone Peter Reistad, Spencer Mark Hatch
Validation: Simon James Walker
Visualization: Simon James Walker
Writing – original draft: Simon James Walker
Writing – review & editing: Simon James Walker, Karl Magnus Laundal, Jone Peter Reistad, Spencer Mark Hatch, Anders Ohma

The Ionospheric Leg of the Substorm Current Wedge: Combining Iridium and Ground Magnetometers

Simon James Walker[1], **Karl Magnus Laundal**[1], **Jone Peter Reistad**[1], **Spencer Mark Hatch**[1], **Anders Ohma**[1], **and Jesper Gjerloev**[1,2]

[1]Department of Physics and Technology, University of Bergen, Bergen, Norway, [2]JHU/APL, Laurel, MD, USA

Abstract Utilizing magnetic field measurements made by the Iridium satellites and by ground magnetometers in North America we calculate the full ionospheric current system and investigate the substorm current wedge. The current estimates are independent of ionospheric conductance, and are based on estimates of the divergence-free (DF) ionospheric current from ground magnetometers and curl-free (CF) ionospheric currents from Iridium. The DF and CF currents are represented using spherical elementary current systems (SECS), derived using a new inversion scheme that ensures the current systems' spatial scales are consistent. We present 18 substorm events and find a typical substorm current wedge (SCW) in 12 events. Our investigation of these substorms shows that during substorm expansion, equivalent field-aligned currents (EFACs) derived with ground magnetometers are a poor proxy of the actual FAC. We also find that the intensification of the westward electrojet can occur without an intensification of the FACs. We present theoretical investigations that show that the observed deviation between FACs estimated with satellite measurements and ground-based EFACs are consistent with the presence of a strong local enhancement of the ionospheric conductance, similar to the substorm bulge. Such enhancements of the auroral conductance can also change the ionospheric closure of pre-existing FACs such that the ground magnetic field, and in particular the westward electrojet, changes significantly. These results demonstrate that attributing intensification of the westward electrojet to SCW current closure can yield false understanding of the ionospheric and magnetospheric state.

Plain Language Summary With a new inversion scheme we resolve the full current based on ground and space magnetometers and spherical elementary current systems We introduce a new inversion scheme for spherical elementary current systems to resolve the full current using ground and space magnetometers.

1. Introduction

Magnetospheric substorms are dynamic events encompassing a range of phenomena surrounding the deposition of stored magnetic energy from the magnetotail into the ionospheric plasma environment (Kepko et al., 2015). The ionospheric currents are constructed from and structured by both the coupling of the interplanetary magnetic field with the magnetosphere and by nightside activity. In particular, substorms are responsible for large variations in the strength and extent of the current systems in the region of the substorm onset (Dungey, 1963; Milan et al., 2017). Much of our understanding of the ionospheric currents in the spatial and temporal vicinity of substorms is restricted to what can be inferred from equivalent currents derived with ground magnetometers.

A key current system involved in a substorm is the substorm current wedge (SCW) where FACs connect a westward horizontal cross tail current to a westward horizontal current in the ionosphere (Coxon et al., 2018; Kepko et al., 2015; McPherron et al., 1973). The true nature of the SCW remains a matter of debate. The original proposal is a single current system that comprises a loop, but more recent theories have suggested a double loop system or even an ensemble of current loops referred to as wedgelets (Gjerloev & Hoffman, 2014; Liu et al., 2015; Ohtani & Gjerloev, 2020). Discussion as to whether the SCW is a development of the Region 1 and 2 currents or its own distinct current system is ongoing. A full picture of the SCW formation and its dynamics is important to understanding how the magnetotail plasma environment develops after the closure of magnetic flux in the tail (Kepko et al., 2015).

The ionospheric current can be described by the sum of its DF and curl-free (CF) components where at high latitudes the magnetic field of the CF currents is considered negligible on ground (Boström, 1964; Fukushima, 1994). Green et al. (2007) had the goal of estimating the global scale Pedersen and Hall conductance. In their steps to achieve this they derived the full ionospheric current, relying on ground magnetometers to measure the

DF horizontal currents and the magnetometers on board the Iridium satellite constellation to measure the CF current system. Green et al. (2007) were restricted by a 1-hr window in order to collect enough measurements for a robust spherical harmonic fit. Similarly, the Active Magnetosphere and Planetary Electrodynamics Response Experiment (AMPERE) project takes advantage of the magnetometers on board the Iridium satellite constellation. AMPERE estimates the FACs on a global scale using spherical cap harmonics and uses a window of only 10 min, yielding a much improved picture of the temporal variability of the FACs (Anderson et al., 2014; Coxon et al., 2018). However, absent any additional information about the horizontal ionospheric current, information about FACs is insufficient for reliable identification of the SCW current system. Similarly to Green et al. (2007) the spherical cap harmonics used in AMPERE require a global fit and the estimates in the region of the SCW will be affected by distant measurements.

The global nature of these approaches is effective when one wishes to examine global current systems, but represents a limitation in the study of more localized phenomena such as the SCW. Furthermore, the 1-hr window makes identification of SCW formation (timescales of minutes) and subsequent analysis of its development impossible.

Ground-based magnetometers have been used to monitor the DF currents for a long time (Harang, 1946). Existing networks provide global coverage and continuous measurements in the auroral zone and are frequently used to detect the onset and phases of substorms (Forsyth et al., 2015; McPherron, 1970; Newell & Gjerloev, 2011; Ohtani & Gjerloev, 2020). The ground magnetic field disturbances are often visualized and modeled as an equivalent electric current on a spherical shell that represents the ionosphere. At high latitudes, where magnetic field lines are radial, this equivalent current coincides with the divergence-free current (Boström, 1964; Vasylinas, 2007). Mathematically, the divergence-free current has no connection to the field-aligned current; however, when combined with physics, we can use it to obtain knowledge about the full 3D current, as outlined below, following Amm et al. (2002).

The height integrated horizontal current can be uniquely decomposed as the sum of divergence-free and curl-free currents, so the curl of the current is the curl of the divergence-free current. The vertical curl of the equivalent/divergence-free current can therefore be related to the electric field in the neutral frame $\vec{E}$, and Hall and Pedersen conductance Σ_H and Σ_P, using the ionospheric Ohm's law:

$$\hat{r} \cdot \left(\nabla \times \vec{J_h}\right) = -\nabla\Sigma_H \cdot \vec{E} - \Sigma_H \nabla \cdot \vec{E} - \hat{r} \cdot \left(\vec{E} \times \nabla\Sigma_P\right), \tag{1}$$

where we have assumed that the Earth's main magnetic field points radially downwards, corresponding to the polar Northern hemisphere. On the other, hand, the divergence of the ionospheric Ohm's law gives the radial (field-aligned), current,

$$\nabla \cdot \vec{J_h} = -j_r = \nabla\Sigma_P \cdot \vec{E} + \Sigma_P \nabla \cdot \vec{E} - \hat{r} \cdot \left(\vec{E} \times \nabla\Sigma_H\right). \tag{2}$$

We see that Equation 1 resembles Equation 2, and if $\hat{r} \cdot (E \times \nabla\Sigma_{P,\,H}) = 0$ and $\Sigma_H = \alpha\Sigma_P$, the curl and divergence of $\vec{J}$ are related by the conductance ratio $\alpha = \Sigma_H/\Sigma_P$ such that the radial current density

$$j_r = -\nabla \cdot \vec{J_h} = \frac{1}{\alpha}\hat{r} \cdot \left(\nabla \times \vec{J_h}\right). \tag{3}$$

Therefore, if the assumptions about conductance given above are valid the polarity and structure of the FACs can be derived using ground based magnetic field measurements by calculating the curl of the equivalent current (Laundal et al., 2022; Weygand & Wing, 2016). We refer to the curl of the equivalent current as the equivalent field-aligned current (EFAC). Even without the assumptions mentioned above, Equation 1 can be used to infer the electric field and FACs, in a mathematically more complicated way: Equation 1 defines a partial differential equation which, if Σ_P, Σ_H, and the curl of **J** are known, can be solved for an electric potential, which in turn can be used with Equation 2 to calculate the FAC. This is known as the Kamide-Richmond-Matsushita technique (Kamide et al., 1981).

Weygand and Wing (2016) and Weygand et al. (2021) used the assumptions that $\hat{r}\cdot(E\times\nabla\Sigma_{P,H})=0$ and $\Sigma_H=\alpha\Sigma_P$ to estimate the FACs from ground magnetometers and describe the Region 1 and 2 current systems. This approach is however only valid to the extent that the assumptions themselves are valid. These assumptions therefore place sweeping constraints on the applicability of this approach. Schillings et al. (2023) used auroral images and particle flux measurements to infer the location of upward and downward FACs and ground magnetometers to estimate the DF currents. Like Weygand and Wing (2016); Weygand et al. (2021), however, they were unable to estimate the full horizontal current and therefore the full current wedge system.

Much like prior work we utilize the magnetometers on board the Iridium constellation in order to estimate the CF currents and ground magnetometers are used to estimate the DF currents. Taking advantage of the DF and CF spherical elementary current systems (SECS) basis functions we are able to estimate these currents regionally. Following the AMPERE approach we use a time window of 10 min to ensure we have enough Iridium magnetic field measurements within the region of interest. We are therefore unable to resolve temporal variations under 10 min. Using a consistent inversion scheme across the DF and CF systems and across case studies we are able to robustly and coherently estimate the total ionospheric current and make event-based comparisons. Furthermore, we compare the ground-based EFAC with the space-based FACs to investigate when the EFAC is a good proxy for FACs, and therefore where and when the required conductance assumptions hold.

In Section 2, we introduce the space and ground magnetic field measurements we use in our estimates of the ionospheric current. We go on to describe the SECS technique and regularization approach we use to solve the under determined inverse problem, explaining clearly how we settle on the scaling of the regularization used. Finally, we present two examples where we compare our estimates for the CF currents with the AMPERE estimated FACs and an associated CF horizontal current. In Section 3 we present a time series from a substorm showing the formation of the SCW and how the EFAC differs from the FAC. We then show current estimates from the expansion phase of 18 different substorms. In Section 4 we discuss the cause of the differences in the EFACs and FACs through the use of the ionospheric Ohm's law. We go on to describe the challenges of understanding the SCW from only ground based magnetometers.

2. Method

In this section we first give a brief overview of SECS and introduce the linear relation between the model amplitudes and magnetic field measurements (Section 2.1). Next we outline the regularization scheme used to solve this under-determined inverse problem (Section 2.2). To demonstrate the appropriateness of the regularization scheme and its scaling we estimate the ionospheric current for two extremely different events (Section 2.3). Finally, we compare our estimates of the CF currents with FACs estimated by AMPERE and its associated horizontal CF current, and demonstrate our estimates of the full ionospheric current.

To estimate the total ionospheric current we make use of two different sets of magnetic field measurements. The DF current is estimated using ground magnetometers in North America. The ground magnetic field measurements are retrieved from SuperMAG where IGRF is used to transform the measurements from local magnetic to the geographic co-ordinate system (Gjerloev, 2012). We select sites that are within the limit shown in Figure 1 and have data within a ten minute window. The mean measurement for each site is then used for the estimation of the DF current. The CF current is estimated using magnetometers on board the Iridium constellation of satellites that have been pre-processed by AMPERE (Anderson et al., 2002, 2014, 2021; Waters et al., 2001, 2020). Iridium data is selected when it is within the limit shown in Figure 1 and within a ten minute window.

2.1. Spherical Elementary Current Systems (SECS)

We use Spherical Elementary Current Systems (SECS) to derive the CF and DF ionospheric currents. The CF and DF currents can be expressed as the sum of individually scaled CF and DF basis functions, respectively, where the scales are found using measurements of the perturbed magnetic field (Amm, 1997; Amm & Viljanen, 1999; Vanhamäki & Juusola, 2020). In this section we summarize the SECS method and basis functions.

Above the ionosphere, the magnetic field can be modeled as being the product of FACs that close in a 2D ionosphere via a horizontal CF current system and a DF current system within the same 2D ionosphere (Laundal et al., 2016). For radial field lines the geometry of the FAC + CF current system is such that it produces no magnetic signature below the ionospheric current layer (Boström, 1964). In this study we place the 2D

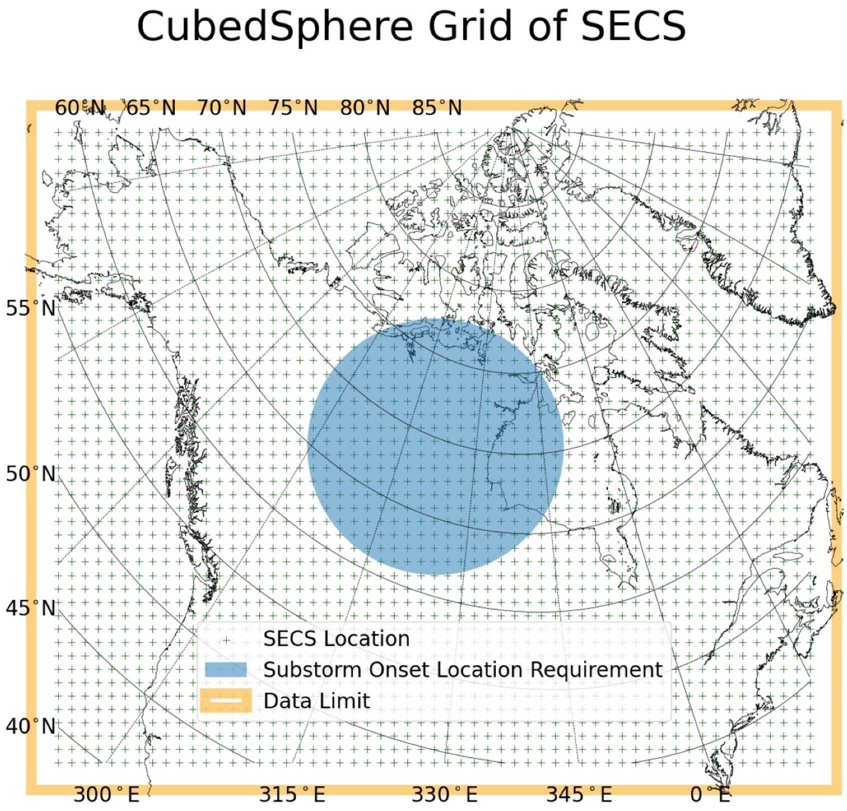

Figure 1. The cubed sphere grid on which SECS basis function are placed is shown using green crosses. The outer boundaries within which data are used in the inversions is shown with an orange line. The blue circle indicates the region where the substorm onsets must occur for the event to be used in this study.

ionospheric current layer at 110 km, the approximate altitude at which the Hall conductance peaks. This means the magnetic field signature of the DF current is significant on ground but negligible at the altitude of the Iridium constellation (≈790 km). We can therefore model the CF and DF currents independently using Iridium magnetometer data and ground based magnetic field measurements, respectively.

Using the sum of appropriately scaled DF SECS basis functions at radius R, the total DF surface current density can be written as

$$\vec{J}^{DF}(\vec{r}) = \sum_i \frac{I_i^{DF}\hat{e}_{\phi_i}}{4\pi R}\cot\left(\frac{\theta_i}{2}\right), \tag{4}$$

where $\vec{r}$ is the location on the sphere where the current is estimated. I_i^{DF} is the amplitude of a DF SECS, $\hat{e}_{\phi_i}$ is a unit vector eastward in the SECS frame and θ_i is the angular distance between the location of the DF SECS basis function and $\vec{r}$. Similarly, the sum of appropriately scaled CF SECS basis functions at radius R can describe the horizontal surface current density component of a CF current system

$$\vec{J}^{CF}(\vec{r}) = \sum_i \frac{I_i^{CF}\hat{e}_{\theta_i}}{4\pi R}\cot\left(\frac{\theta_i}{2}\right). \tag{5}$$

where I_i^{CF} is the amplitude of a CF SECS, $\hat{e}_{\theta_i}$ is a northward unit vector in the SECS frame and the remaining variables have the same interpretation as those in Equation 4. The amplitudes of the CF SECS systems are the radial FACs connecting to the CF currents from infinity. When divided by the corresponding SECS grid cell area, these amplitudes may be viewed as estimates of the local FAC density.

Amm and Viljanen (1999) derived the magnetic field of each DF and CF SECS:

$$\Delta B_{\theta_i}^{DF}(\theta_i, r) = \frac{-\mu_0 I_i^{DF}}{4\pi r \sin\theta_i} \begin{cases} \dfrac{s - \cos\theta_i}{\sqrt{1 + s^2 - 2s\cos\theta_i}} + \cos\theta_i & r < R \\ \dfrac{1 - s\cos\theta_i}{\sqrt{1 + s^2 - 2s\cos\theta_i}} - 1 & r > R \end{cases} \tag{6}$$

$$\Delta B_{\phi_i}^{DF}(\theta_i, r) = 0 \tag{7}$$

$$\Delta B_r^{DF}(\theta_i, r) = \frac{\mu_0 I_i^{DF}}{4\pi r} \begin{cases} \dfrac{1}{\sqrt{1 + s^2 - 2s\cos\theta_i}} - 1 & r < R \\ \dfrac{s}{\sqrt{1 + s^2 - 2s\cos\theta_i}} - s & r > R \end{cases} \tag{8}$$

$$\Delta B_\phi^{CF}(\theta_i, r) = \frac{-\mu_0 I_i^{CF}}{4\pi r} \begin{cases} 0 & r < R \\ \cot\left(\dfrac{\theta_i}{2}\right) & r > R \end{cases} \tag{9}$$

where $s = \min(r, R)/\max(r, R)$.

Describing the magnetic field from the DF SECS both above and below the SECS layer is important when using ground based magnetometers ($r = R_E$) as the total perturbed magnetic field on ground is due to the sum of ionospheric ($R_E < R_I$) and telluric sources ($R_E > R_T$) which can also be modeled with SECS. Equation 9 illustrates Fukushima's theorem, that the magnetic field below the CF ionospheric surface density current layer is negligible (Boström, 1964; Fukushima, 1976; Marklund et al., 1982).

From Equations 6 to 9 it is evident that the relationship between the magnetic field measurements and the scaling of each CF and DF SECS is linear:

$$G\vec{m} = \vec{d}, \tag{10}$$

when we estimate the DF current, $\vec{m}$ consists of DF SECS amplitudes and $\vec{d}$ of ground magnetic field vector components with units of Tesla, while the matrix G is based on Equations 6–8. When we estimate the CF current, $\vec{m}$ consists of CF SECS amplitudes, $\vec{d}$ consists of Iridium magnetic field measurements with units of Tesla, and the matrix G is based on Equation 9.

As discussed by Walker et al. (2023), the choice of grid in a SECS-based approach is important. As we want to resolve the DF and CF currents in a similar manner we use the same grid for both the DF and CF SECS. Following previous studies such as Walker et al. (2023) and Laundal et al. (2021), we use a cubed sphere grid (Ronchi et al., 1996; Sadourny, 1972). Our grid, shown in Figure 1, is centered at 258° geographic longitude (glon) and 61° geographic latitude (glat) with an average grid spacing of 100 km, and orientated approximately along magnetic meridians. The grid has $N = 2{,}736$ cells, each with a DF and CF elementary current system at an altitude of 110 km. To account for induced currents, we place an additional layer of DF SECS below the ground. Instead of treating these additional SECS amplitudes as free parameters, we use the mirror current technique (Juusola et al., 2016), where each telluric current system amplitude depends exactly on the overhead current system, and place them at such a depth that the radial magnetic field from the telluric SECS cancels the radial magnetic field from the ionospheric SECS at a depth of 500 km. In the EFAC and in estimates of total ionospheric current density, only the DF ionospheric current from SECS at 110 km is used.

2.2. Solving the Inverse Problem

Due to the scarcity of both space- and ground-based magnetometer measurements, for all events addressed in this study the inverse problems are under-determined. In prior studies, Walker et al. (2023); Laundal et al. (2021), regularized least-squares has been used to guide the solution to a more physical result using prior information such as the expected structure. The minimization of the cost function

$$f = ||G\vec{m} - \vec{d}\,||^2 + \lambda_1||L\vec{m}\,||^2 + \lambda_2||L_e\vec{m}\,||^2 \tag{11}$$

gives the solution of the model amplitudes $\vec{m}$. The first term represents the total misfit between the measurements $\vec{d}$ and the model predictions $G\vec{m}$; for $\lambda_1 = \lambda_2 = 0$ (i.e., in the absence of any regularization). Minimizing this term produces the least-squares solution for which the total model-data misfit is minimized. The second term represents the difference between neighboring cells, and its presence encourages solutions with large-scale, coherent structures; its importance is scaled by λ_1, a value that must be chosen. This regularization term is in contrast to prior studies where the first regularization term minimizes the euclidean norm of $\vec{m}$ (Laundal et al., 2021; Walker et al., 2023). The final term represents the gradient of the SECS amplitudes in the magnetic east direction, and encourages solutions that are aligned in the east-west direction; it is scaled by λ_2, a second value to be chosen. This same east-west regularization scheme has been implemented in a number of prior SECS-based studies (Laundal et al., 2021; Walker et al., 2023).

To make the amount of regularization consistent across events for given values of λ_1 and λ_2, we divide the regularization terms $||L\vec{m}\,||^2$ and $||L_e\vec{m}\,||^2$ by the median of G^TG for each inversion. This scaling accounts for changes in model geometry due to variations in magnetometer sites or Iridium data locations. This re-scaling also ensures that the regularization is the same for the DF and CF inversions, encouraging similar spatial scales and structure as long as λ_1 and λ_2 are the same for the DF and CF inversions. Through experimentation and studying a number of events we find that $\lambda_1 = 10^3$ and $\lambda_2 = 5 \times 10^4$ are appropriate choices for these parameters, these values are appropriate for magnetic field measurements given in Tesla and the specific grid used for the placement of the SECS. These values are used for both the DF and CF inversions and for all events presented in this study.

2.3. Examples

To demonstrate the technique and how we chose the scaling of the regularization we present two very different events in Figures 2 and 3.

Figure 2 is an example that demonstrates an electrojet structure in the DF SECS (top row) that is structured east-west. Similarly the CF SECS (bottom row) shows FACs structured east-west resembling the Region 1 and 2 current systems apart from an interface between opposing polarity FACs at around 330° MLon. The spatial scales are very similar between the DF and CF SECS models, which we can see most clearly in the agreement in the location and size of the Region 1 and 2 currents (as seen by the FACs in CF SECS and the EFACs in DF SECS) in areas away from the center of the plots (between 250° and 310° MLon and between 0° and 65° Mlon) and below 80° MLat. In the left panels we can see a high goodness of fit as there are clear similarities between the measured magnetic field (red arrows, for the DF and CF inversion, and colored dots for the DF inversion) and modeled magnetic field (black arrows, for the DF and CF inversion, and also colored background, for the DF inversion). At around 65° MLat there is opposing direction of FACs to the east and west of 330° MLon despite the east-west gradient regularization applied in the inversion. The EFACs on the other hand do not display any significant east-west gradients. These differences demonstrate that (a) the regularization is not so strong as to defy the measurements, and (b) the east-west structure in the EFACs is not an artifact of the inversion.

Figure 3 shows another example of the DF and CF SECS inversion. Treating the data in the same manner as in Figure 2, we use Iridium and ground magnetometer data from the 12th of January 2011 from 05:15 to 05:25 UT. Structures in the FACs and EFACs are not as clearly east-west aligned in this example which shows that the east-west regularization is not so strong as to suppress significant structures in the longitudinal direction. Once again the left panels show a good fit between the measured and modeled magnetic field. Furthermore, there is a very good agreement between the FACs and the EFACs, which again shows that the regularization encourages similar scale sizes in the DF and CF inversions. Taken together, Figures 2 and 3 justify the choice of regularization scaling parameters.

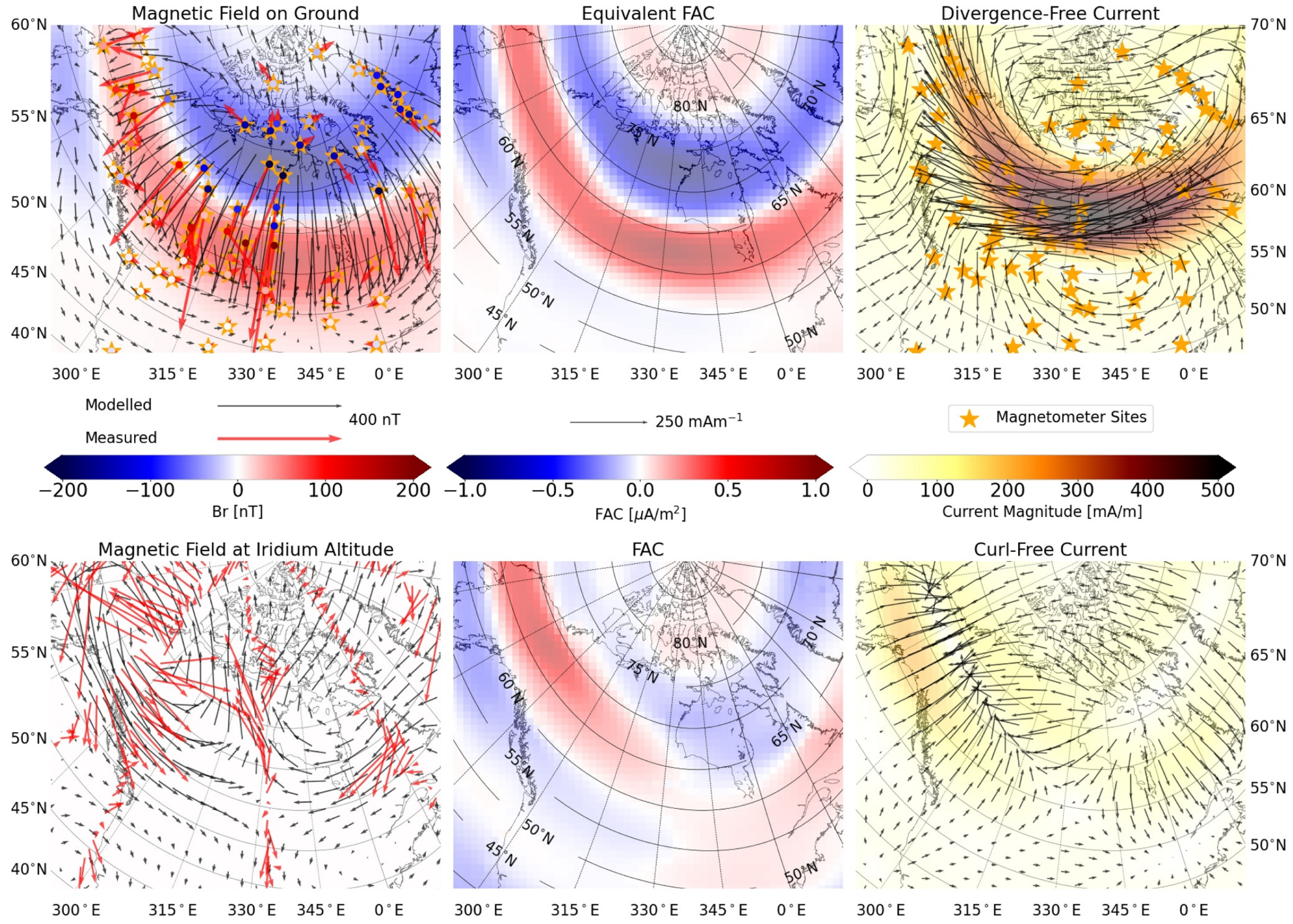

Figure 2. Measured and modeled magnetic fields of DF (top row) and CF (bottom row) currents based on data from 1 June 2011 between 07:56 and 08:06 UT. The DF SECS inversion is based on the mean magnetic field measurements from ground magnetometers, and the CF SECS inversion is based on Iridium magnetic field measurements within two grid cells of the grid (limit show as an orange line in Figure 1). Left panels show the input magnetic field measurements and modeled magnetic field at the same altitude as the measurements. Measured horizontal components are shown as red vectors, and modeled as black vectors. The color in the top left panel represents the modeled vertical magnetic field component, and the dots in the stars, which denote measurement locations, represent the measured radial magnetic field. The middle panels show the SECS amplitudes divided by grid cell area producing EFACs for the DF SECS and FACs for the CF SECS. The right panel shows the modeled horizontal ionospheric currents as black vectors and their amplitude represented by the background color.

2.4. AMPERE Comparison

Much like this study, the AMPERE project utilizes the magnetic field measurements from the Iridium constellation of satellites. In contrast to this study, they use spherical cap harmonics to model the FACs in the entire polar region (Anderson et al., 2002, 2014, 2021; Waters et al., 2001, 2020). Figure 4 shows the two events presented in Figures 2 and 3. The top row shows the FACs from AMPERE, regridded onto the SECS grid using linear interpolation (using the scipy regrid function (Virtanen et al., 2020)), as the background color. Using the CF SECS basis functions and AMPERE FACs we also estimate the horizontal CF current and show it as black vectors. The middle row shows the CF current using the SECS method described in this study. The bottom shows the full ionospheric current where the FACs are derived from the CF SECS amplitudes and the horizontal current is the sum of the SECS estimated DF and CF currents.

The example in the right panels shows that there is a significant difference in the spatial scales produced by AMPERE and the CF SECS inversion. This is expected due to the differences in the two approaches. The example in the left panels show a vortex-like structure where there is a large-scale upward FAC structure centered at around 75° MLat and 21 MLT. The scale size of this structure is similar in both the SECS-derived FACs and the AMPERE FACs. This again confirms that despite differences between AMPERE and the CF SECS FACs there is a significant level of consistency that demonstrates the validity of our approach.

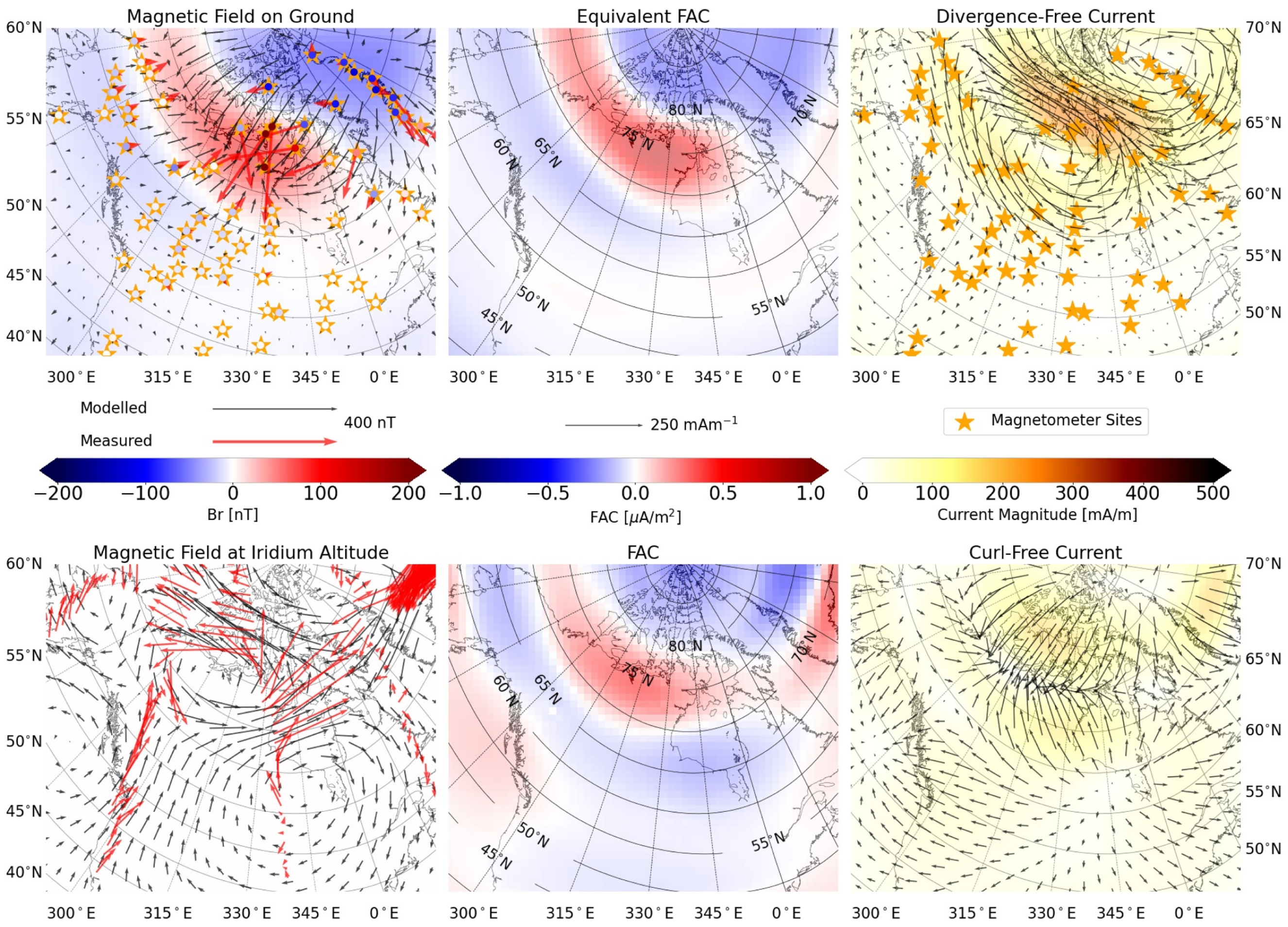

Figure 3. The same as Figure 2 but using mean ground magnetometer measurements and Iridium magnetometer measurements from the 12th of January 2011 between 05:15 and 05:25 UT.

In both examples the importance of the use of the same regularization scheme for the DF and CF SECS inversions is highlighted. In the left panel the full horizontal current represents a vortex surrounding the upward FAC structure. Such circular currents require a coherence between DF and CF currents that can only be achieved with similar spatial scales. The right example shows a SCW where the full ionospheric current connects the downward FACs east of 1 MLT with the upward FACs west of 1 MLT. One can see in Figure 2 that although the EFACs and FACs are not aligned the similar spatial scales are still necessary between the DF and CF horizontal currents to produce this large scale SCW. Finally, we reiterate that differences between AMPERE and CF SECS FACs merely indicate different choices in methodology. The CF SECS-based methodology that we employ is fit for the purpose of combining the DF and CF currents and for resolving the SCW or current structures of similar spatial scales.

3. Results

In this section we present estimates of the total ionospheric current during a set of substorms, using the technique described above where we model the horizontal DF and CF currents separately. Substorms are chosen if they are identified by all three of the Newell and Gjerloev (2011), Forsyth et al. (2015), and Ohtani and Gjerloev (2020) substorm lists and within the years 2011 and 2012. Additionally, the onset location, determined by the magnetometer that contributes to the SML index at the time of onset (provided by Forsyth et al. (2015)), must occur within a radius of ten grid cells from the center of the SECS grid (shown as blue circle in Figure 1) and between 21 and 1 MLT. We use three lists to reduce the likelihood of a false substorm detection and apply an onset location restriction to ensure that the current systems surrounding the onset are resolvable and therefore that the SCW, if it exists, can be found.

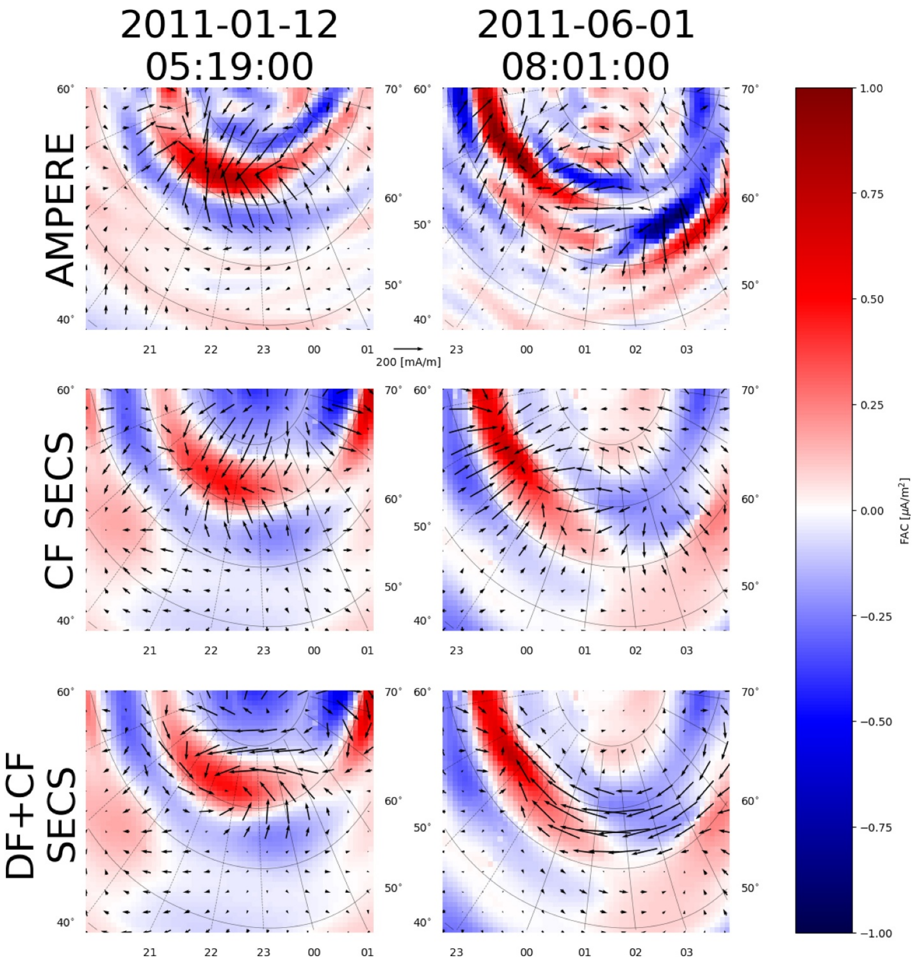

Figure 4. Comparison of the CF current system as interpreted using CF SECS or using AMPERE FAC. The top row shows the AMPERE field aligned currents regridded onto the SECS grid used in this study. Black vectors show the estimated horizontal component of the CF current when AMPERE FACs are translated into CF SECS amplitudes. The middle row shows the CF currents based on the magnetic field measurements from Iridium and the method presented in Section 2. The bottom row shows the total current where the horizontal current is the sum of the DF and CF current and the FAC is based on the CF SECS amplitudes. The left panels shows an event on 12th of January 2011 where Iridium magnetic field measurements between 05:15 and 05:25 UT are used for AMPERE and the CF SECS inversion. The right panels are in the same layout but for observations made on the 1st of June 2011 between 07:56 and 08:06 UT.

3.1. Full Ionospheric Current

3.1.1. Current Wedge Formation and Evolution

Figure 5 shows the time evolution of the total ionospheric current during a substorm on the 1st of June 2011 with onset at 07:51 UT. The left column is based only on ground magnetometers, and shows the total current as the sum of DF SECS and CF SECS, where the latter is calculated from the DF SECS in accordance with Equation 3 with $\alpha = 1$. The EFAC densities are indicated by the background color. The right column shows the total ionospheric current based on both ground and space measurements. Here the FACs, shown by the background color, are based on the Iridium satellite data and the horizontal vector is the sum of the ground-based DF and space-based CF current. The bottom panel shows the SML index (Gjerloev, 2012) over the period of the substorm and dotted vertical lines show the center of the ten minute windows for each panel. The titles to the left of the panels refer to the center of the data window used for the currents shown; for example, Epoch −5 uses data from 10 min prior to substorm onset up to substorm onset.

Prior to the onset of the substorm the FACs and EFACs show some similarity. At Epoch 10 the SCW, which has been formed between 60° and 70° MLat, connects a downward FAC to the east of 1 MLT to an upward FAC west

10.1029/2024JA032414

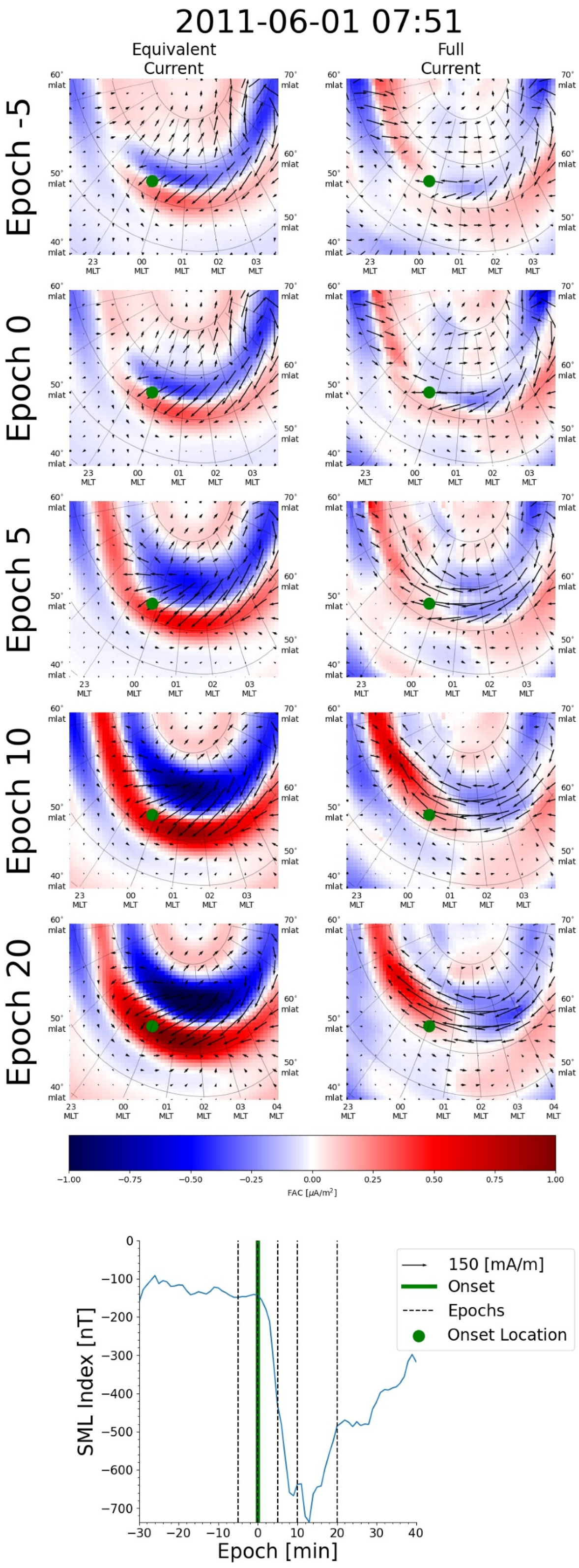

Figure 5. Time series of the total ionospheric current purely determined from ground measurements (left column) and from both ground- and space-based measurements (right column). Epoch refers to the minutes from the substorm onset for the center of the data window used for the inversions (e.g., for Epoch −5 the data window spans from 10 min before the substorm onset up to the time of the onset). The bottom panel shows the SML index from 30 min before the onset up to 40 min after onset. The green dot in each panel shows the location of the substorm onset detected by Forsyth et al. (2015).

of 1 MLT. Around the location of the substorm onset and once the SCW has been formed the similarity between the FACs and EFACs is lost. However, at increasing distance from the substorm onset location, such as before 22 MLT and after 3 MLT, the degree of similarity between the EFACs and FACs is greater. Even prior to substorm onset the full horizontal current derived from only ground based magnetometers (left column) is clearly different from the full horizontal current based on data from both ground and space (right column). This demonstrates the difficulty of obtaining a reliable estimate of the total horizontal ionospheric current on the sole basis of ground magnetometers, even when the FACs and EFACs exhibit similar structures.

3.1.2. Snapshots of the Substorm Current Wedge

The substorm criteria we apply yield 18 substorm events. Through manual examination of the substorms we find that the SCW generally forms around Epoch 10 to 15. Therefore, we present the ionospheric currents at Epoch 20 to give adequate time for the SCW to form.

Figures 6–8 show all 18 substorms at epoch 20 min, where the data used in the inversion spans from epoch 15 min to epoch 25 min. The left panel shows the SML index over the period of the substorm, where a green dashed vertical line marks the time of substorm onset and the time span of data used in the inversions is highlighted in orange. The middle panels show an equivalent total ionospheric current where the DF SECS amplitudes and are used to scale the CF SECS ($\alpha = 1$ in Equation 3). The total horizontal current is then the sum of the DF current and this equivalent CF current, represented by the black vectors. The background color shows the corresponding CF SECS amplitudes divided by grid cell area (the EFAC). The right panels show the full ionospheric current as black vectors, calculated as the sum of the ground-based DF and space-based CF current. The background color shows the FACs, based on the CF SECS amplitudes estimated with Iridium satellite data.

The substorm event on the 1st of June 2011 (second row in Figure 6, identical to last row of Figure 5) shows a clear SCW between 60° and 70° MLat where a horizontal westward current connects downward and upward FACs east and west of 1 MLT respectively, as discussed in Section 3.1.1. We consider this current wedge a depiction of a typical current wedge structure. The horizontal component of the current wedge is aligned toward magnetic west connecting clearly defined downward and upward FACs in the east and west respectively. Based on this description of a typical SCW, Table 1 lists the substorm events in this study denoting whether the current wedge has typical or atypical structure. We see that two thirds of the substorms presented in this study exhibit a typical current wedge, although width, location and strength of the current wedge can vary. For these events, the upper limit of the current wedge width is around 10° MLat and the lower limit is just a few degrees MLat. Furthermore, in these events as we increase in distance from the SCW the FACs return to a more typical region 1 and 2 current structure and become more similar to the EFACs.

The event on the 22nd of June 2011 (top row in Figure 8) is considered atypical. Much like the typical events, FACs are aligned east-west. However, they are orientated such that the upward FACs are northward of the downward FACs and the interface between them occurs at $\sim 72°$. Consequently, the horizontal connecting current is directed northward.

The event on the 4th of May 2011 (second row in Figure 8) is also considered atypical because the FACs are not well defined and the overall current system is weak. The reason for this and for the current wedge being so weak and narrow can be at least partially inferred from the SML index over the period of the substorm: At the time of onset there is a weak but sharp decline in SML index that triggers the substorm algorithms, with a later and more dramatic decline in the SML index occurring at Epoch 20. In this event it appears that the weak and narrow SCW is likely related to the first and weaker dip in the SML index. At Epoch 30 a clear typical SCW appears, suggesting that either that mechanism behind the initial SCW was weak and affected similarly as the SML index or the required mechanism began during the second stronger dip and the SCW required more time to form. Given that the typical events do not show a weak and narrow SCW prior to the formation of the clear SCW, it is most likely that the mechanisms surrounding the first onset-related dip in the SML index had little energy and formed a weak and narrow SCW, and the mechanisms surrounding the subsequent stronger dip provided more energy allowing a strong typical SCW to form.

The events on the 3rd of June 2012 and on the 29 December 2011 (respectively third and fourth rows in Figure 8) are considered atypical due to the structure of FACs and horizontal currents but have westward connecting currents around the location of substorm onset. 3rd of June 2012 is considered atypical because the upward FACs

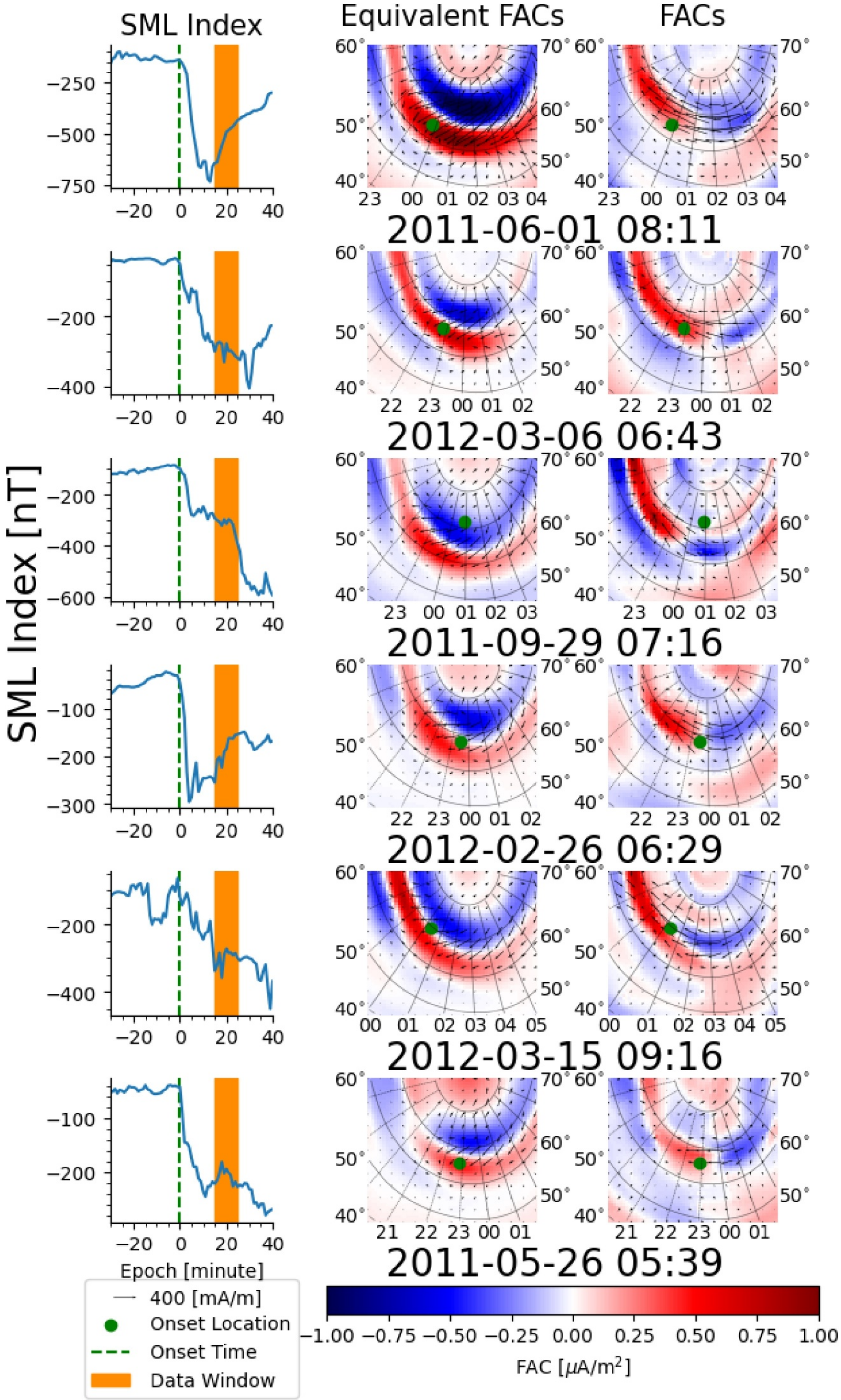

Figure 6. Full ionospheric current for six substorms classified as “typical.” Left panels show the SML index from 30 min before to 40 min after the substorm. Middle panels show the full ionospheric current when DF SECS amplitudes are used to interpret the FACs, DF and CF currents. Right panels show the full ionospheric current when CF SECS are used to interpret the FACs and horizontal currents are DF currents (based on DF SECS and ground-based measurements) plus CF currents (based on CF SECS and Iridium measurements). Each row shows a different substorm using measurements from a 10-min window centered at substorm epoch twenty minutes (shown in orange in the left panels). For each panel the substorm onset occurs 20 min prior to the indicated time (e.g., for the top panel substorm onset occurs at 06:23 UT). The green dot in each panel shows the location of the substorm onset detected by Forsyth et al. (2015).

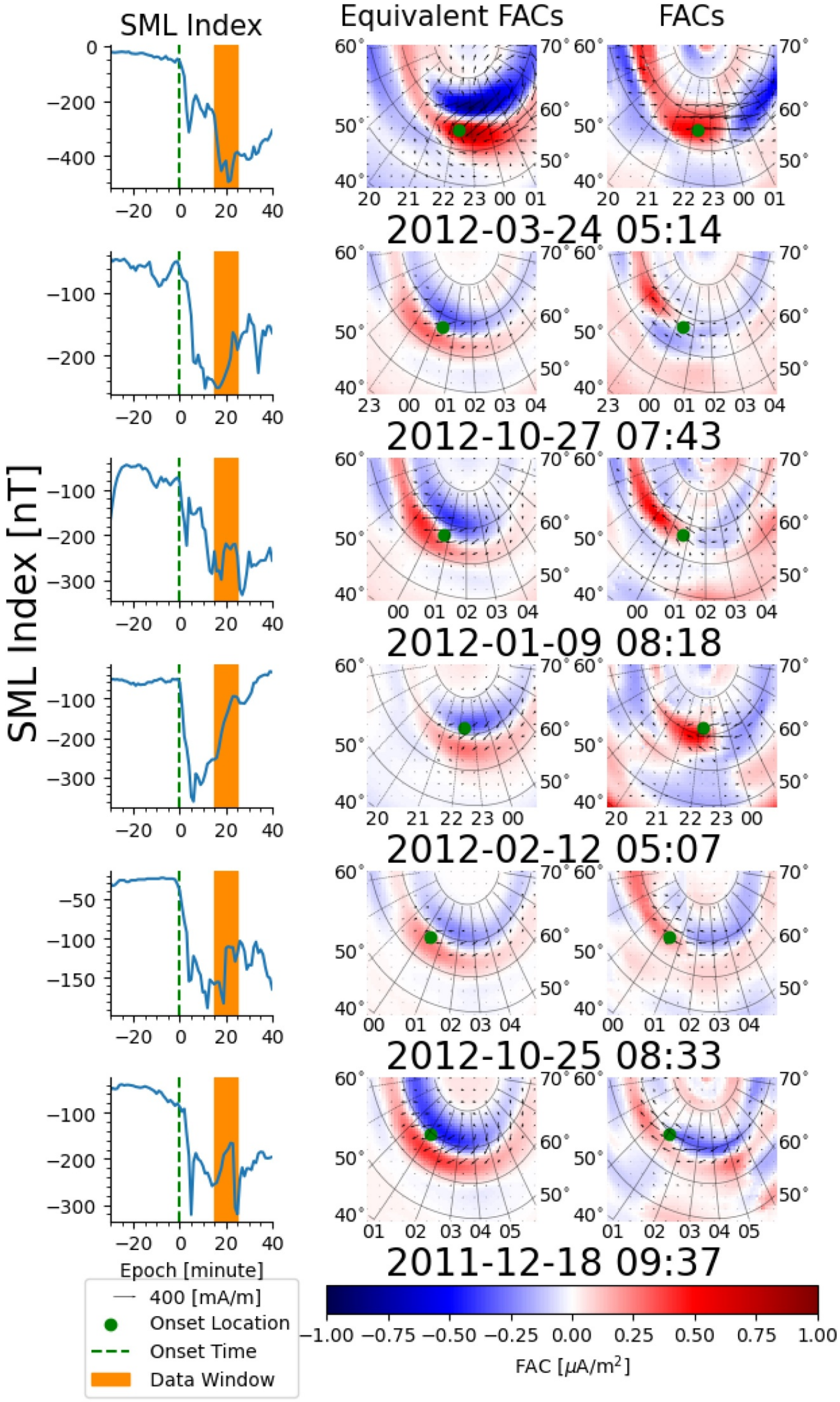

Figure 7. Six different substorm events classified as "typical" in the same layout as Figure 6.

close to the onset location are as weak as and in some cases weaker than the background. Furthermore, the upward region 1 FACs are weak and poorly distinguished. 29 December 2011 is considered atypical because there is significant north-south interface between the upward and downward FACs with a connecting southward horizontal current. The EFACs in these events demonstrate a greater similarity with the FACs close to the current wedge than the typical events. The atypical event on the 29th of January 2012 (fifth row in Figure 8) shows no clear formation of a current wedge, and as expected by the strength of the SML index, the currents are very weak compared to the other events. Much like Figure 5 pre-onset and in the two events just mentioned (3rd of June 2012

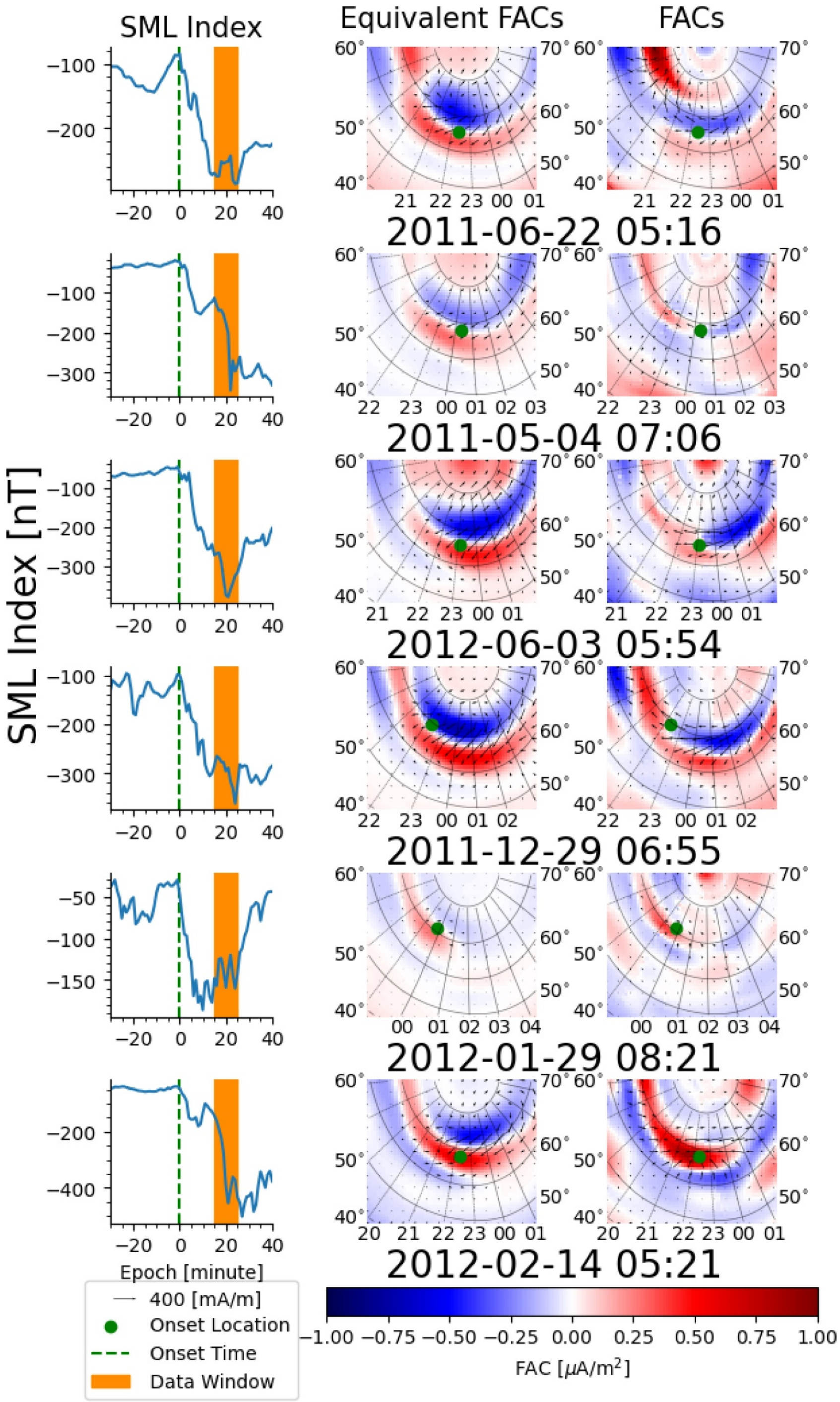

Figure 8. Six different substorm events classified as "atypical" in the same layout as Figure 6.

and 29th of December 2011) the EFACs and FACs are incredibly similar, apart from poleward of 80° MLat where ground magnetometer sites are lacking.

4. Discussion

We have outlined and demonstrated a methodology that allows us to investigate the total ionospheric current in close spatial and temporal proximity of substorm onsets. The inversion scheme, which relies on Tikhonov regularization as described in Section 2.2, is consistent for all events and for both the DF and CF SECS, as shown in

Section 2. Using this scheme, in Section 3 we have identified when the SCW forms during a substorm and tested the validity of resolving the total ionospheric current purely from ground based magnetometers during substorms.

The EFAC approach described in the Introduction has often been used to obtain a proxy for the true FACs (Nishimura et al., 2020). However we find that the degree of similarity between the ground-based EFACs and FACs estimated with satellite magnetometers varies strongly with epoch time relative to substorm onset: Figure 5 shows that prior to onset the structure of the upward and downward EFACs are similar to the space-based FACs but overall the magnitude of the EFACs is higher. Post-onset the similarity between EFACs and space-based FACs rapidly deteriorates with clearly different structures that intensify as the substorm progresses.

Figures 6–8 show snapshots from 18 substorms, based on data 15–25 min after onset. In events that we consider typical there is a classic substorm current wedge with a downward current dawnward of onset, connected by horizontal currents to an upward current on the dusk-side of the onset. The ground-based equivalent current on the other hand, shows clear east-west bands of downward EFACs poleward of upward EFACs. Additionally, we find that spatial proximity to the onset also determines the similarity between the EFACs and space-based FACs, with the similarity being greater with increasing distance from the substorm onset. In order for the EFACs and FACs to become increasingly dissimilar in time there must be a corresponding change in the conductance ratio and gradients, such that the assumptions $E \times \nabla\Sigma = 0$ and $\Sigma_H = \alpha\Sigma_P$ discussed in connection with Equation 3 are no longer valid. During substorms the mismatch between FACs and EFACs becomes significant close to the substorm bulge, but they remain similar away from the onset location. It is sensible to then infer that there is an alteration to the Pedersen and Hall conductance beginning at the time of substorm onset and occurring around the location of the onset.

Table 1
List of Substorm Events Shown in This Study and a Comment on the Current Wedge Structure

Time	Figure number	Typical
2012-03-06 06:23	6	Yes
2011-06-01 07:51	6	Yes
2011-09-29 06:56	6	Yes
2012-02-26 06:09	6	Yes
2012-03-15 08:56	6	Yes
2011-05-26 05:19	6	Yes
2012-03-24 04:54	7	Yes
2012-10-27 07:23	7	Yes
2012-01-09 07:58	7	Yes
2012-02-12 04:47	7	Yes
2012-10-25 08:13	7	Yes
2011-12-18 09:17	7	Yes
2011-06-22 05:56	8	No
2012-06-03 05:34	8	No
2012-02-14 05:01	8	No
2011-12-29 06:35	8	No
2012-01-29 08:01	8	No
2011-05-04 06:46	8	No

Note. The main characteristic of a "typical" substorm current wedge structure is the presence of a clear westward current connecting clearly defined downward and upward FACs eastward and westward respectively.

The changes in conductance that alter the relationship between the EFACs and the true FACs are likely explained by energetic particle precipitation within the substorm auroral bulge. With this in mind Figure 9 tests the impact of an auroral bulge on the EFACs. We first generate a FAC pattern consisting of a typical region 1 and 2 current system (panel A Figure 9). These FACs are produced using the Average Magnetic field and Polar current System (AMPS) model, an empirical model of the polar ionospheric currents based on magnetic field measurements from the *Swarm* and Challenging Minisatellite Payload (CHAMP) satellites (Laundal et al., 2018; Laundal & Toresen, 2018). The AMPS map correspond to a solar wind velocity of 400 kms^{-1}, 0 nT IMF B_y, −5 nT IMF B_z, a dipole tilt of close to 25° and 100 F10.7 cm radio flux. We now wish to calculate the EFAC that would be measured by ground magnetometers, given this FAC pattern and various conductivity maps. To do this we use the ionospheric Ohm's law and the Local Mapping of Polar Electrodynamics (Lompe) technique (Laundal et al., 2022) to solve the current continuity equation, with a boundary condition of zero convection at 50° MLat. With this input, the Lompe technique allows us to calculate the EFACs.

In Figure 9b, we show the Hall and Pedersen conductance based on a model of solar extreme ultra violet (EUV) ionization, as described by Laundal et al. (2022) using the same dipole tilt angle and F10.7 cm solar flux provided to the AMPS model. The corresponding EFAC is shown in Figure 9d. We then repeat this but add a Gaussian function to the solar EUV Hall and Pedersen conductance to replicate the creation of the auroral bulge (shown in Figure 9c).

$$\Sigma_{Bulge} = pe^{-\frac{1}{2}\left(\frac{(\lambda_m-67)^2}{5^2}+\frac{\min\left((\phi-23)^2,\,(24-|\phi-23|)^2\right)}{2^2}\right)} \tag{12}$$

where λ_m and ϕ are magnetic latitude and locale time, respectively, and the amplitude of the Gaussian is placed at $\lambda_m = 67°$, $\phi = 23$, consistent with statistics of substorm onset locations presented by Frey et al. (2004). For the

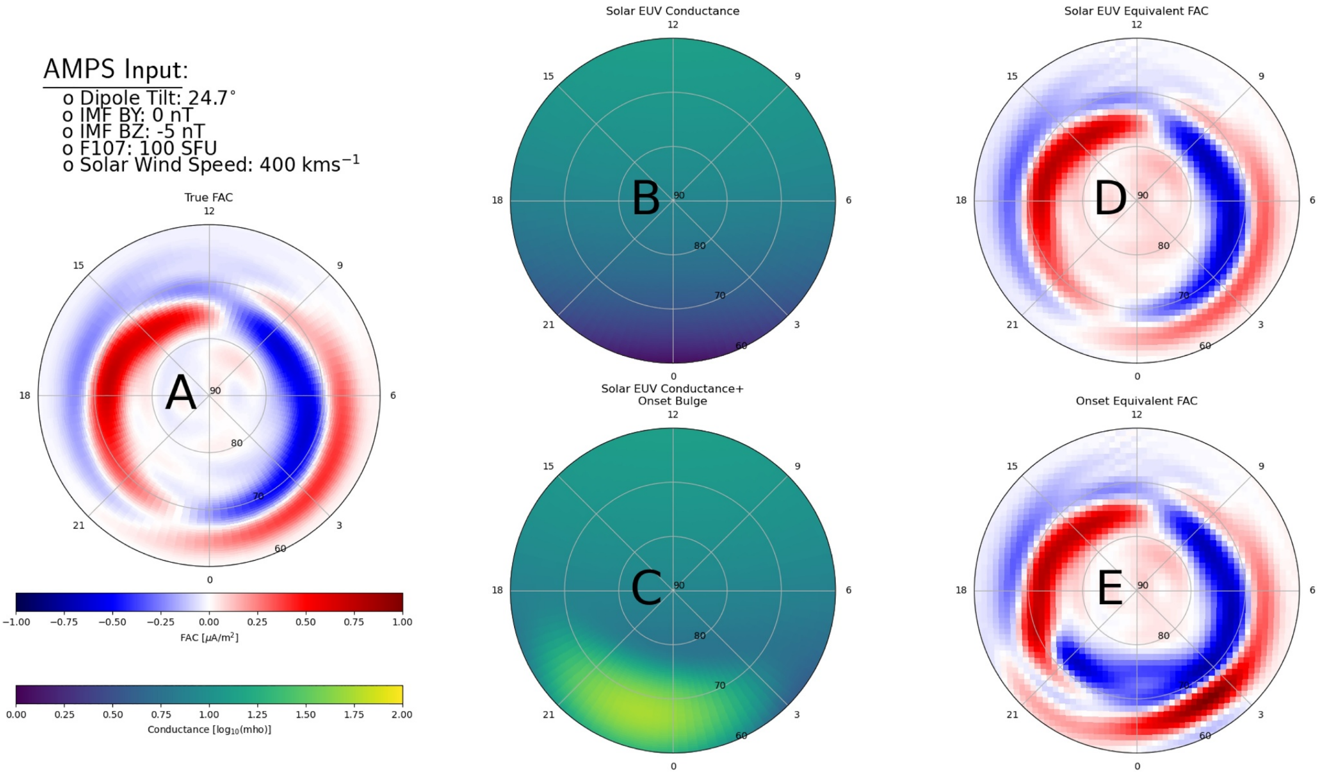

Figure 9. Lompe calculations of the impact of the auroral bulge on the EFACs. Panel A shows an AMPS-determined FAC pattern to replicate a typical steady state FAC system. Panel B shows example Hall conductance created by solar EUV radiation. Panel C shows the Hall conductance using the solar EUV model plus a Gaussian to replicate the substorm auroral bulge. Panel D shows the EFACs for purely solar EUV conductance. Panel E shows the EFACs when the conductance of the auroral bulge is added.

Hall conductance we set its peak value to $p = 55\ \Omega^{-1}$ and the Pedersen conductance $p = 25\ \Omega^{-1}$, consistent with values for substorm conductance presented by Aksnes et al. (2002). Using this conductance model we use Lompe to produce new EFACs shown in panel E of Figure 9. While the approach we use in Figure 9 should not be treated as an exact truth and does not guarantee self-consistency between the conductance and the FACs it is not an unrealistic scenario. In this example we do not allow the FACs to change despite implying energetic particle precipitation in the auroral bulge. This can still occur in a real scenario because as the conductance change only informs us that there are charge particles with motion toward the ionosphere, it does not inform us of the bulk motion of the energetic particles. Therefore, it is entirely possible for energetic particle precipitation to occur without a significant change in the FACs.

It is clear that the auroral bulge causes the EFACs to significantly differ from the true FACs and become overall stronger in the region of the auroral bulge. Stronger EFACs means there is a strengthening of the westward electrojet as a direct result of the auroral bulge and this change in the DF currents causes the region 1 and 2 currents to close through the bulge. The SCW requires an intensification of the FACs, and therefore this intensification of the westward electrojet in Figure 9e is not an indicator of the SCW. Figure 5 shows that this can be the case even in typical events. The westward electrojet intensifies at Epoch 5 (when all ground magnetometer data used in the inversion is at or post substorm onset) but the SCW does not appear until Epoch 10. This means that if one were to use purely ground magnetometers the formation of the SCW could be misidentified.

The typical substorms in Figures 6 and 7 all show similar EFAC structures: a deformed region 1 and 2 current system close to that shown in panel E of Figure 9. The space-based FACs, however, generally show the expected SCW current system. The formation of the substorm current appears to widen and strengthen the region 1 current system while the region 2 current system weakens and moves equatorward or is not visible above the background.

For the atypical substorms shown in Figure 8 the distributions of FAC densities estimated from Iridium satellites are generally very different from each other, while the EFACs evince the same basic pattern: They appear as the deformed Region 1 and 2 currents that we expect from the change in the conductance from the auroral bulge. Given that there is no obviously identifiable SCW in the Iridium-based FACs and in the full (space- and ground-based) horizontal currents and that these currents have incredibly different structures between the events, the similarity of the EFAC densities estimated from ground-based measurements to those in the typical substorm events confirms that the SCW is not required to produce the substorm features seen in the equivalent currents. This reinforces the point made earlier that estimates of ionospheric current system exclusively via ground-based measurements can lead to false detection and interpretation of the SCW.

While there are few studies resolving the full ionospheric current of the SCW, there are similarities between the components of the current that we have shown here with those shown in at least one previous study: Forsyth et al. (2018) report on an intensification of the FACs post onset with a slow decay and stronger upwards FACs compared to downward. This same post-onset intensification can be seen in Figure 5. The typical onset events (Figures 6 and 7) also tend to show stronger upward FACs.

5. Conclusion

A new inversion scheme has been introduced to model the total ionospheric current using simultaneous magnetometer measurements on ground and in space. Consistent data processing across events allows us to compare equivalent FACs (determined via the curl of the ground-based equivalent current) with FACs estimated directly from space-based magnetometer measurements in 18 different substorms. The spatial resolution of our estimates of CF and DF currents is also stable and consistent across all events; this enables robust intra- and inter-event comparison of the spatiotemporal development of the ionospheric current system.

We have also demonstrated that post substorm onset the curl of the horizontal currents, estimated with ground magnetometers and referred to as the equivalent FAC, is in general a poor proxy for the true FACs with increasing spatial proximity to the substorm onset location. Using a ten-minute window for data used in the estimation of the ionospheric current we are able to investigate the evolution of the ionospheric currents on substorm scales. We find that the formation of the SCW is delayed relative to substorm onset and, at the scales that we resolve here, that there are no clear signs of the SCW being composed of wedgelets. Given that the number of space borne magnetometers is the limiting factor in the temporal resolution and spatial scales of the currents estimated, the use of extra satellite magnetometers in future studies can reduce the data window and regularization. This would improve our understanding of the formation and evolution of the SCW and allow us to more fully address the theory of substorm current wedgelets.

Despite its frequent use in the study of the SCW, we have shown that intensification of the westward electrojet as manifested by a drop in the SML index does not necessarily imply an enhancement of the FACs that are an integral part of the formation of the SCW. Such an intensification can occur due to the change in conductance in the expansion phase, changing the current path through the ionosphere but without the formation of the SCW.

Data Availability Statement

The ground magnetometer data has been retrieved from the SuperMAG collaboration: https://supermag.jhuapl.edu/mag, where data from all stations were downloaded as yearly files, in April 2022. The AMPERE field-aligned currents and processed Iridium magnetometer data has been retrieved through the AMPERE project: https://ampere.jhuapl.edu/download/?page=zipDataTab in April 2022. The horizontal currents, FACs and EFACs that have been estimated in this study from epoch −10 to epoch 30 are provided at Walker (2023).

Acknowledgments
This work was funded by the Research Council of Norway, contract 300844/F50, and by the Trond Mohn Foundation. KML was also funded by the European Union (ERC, DynaMIT, 101086985). Views and opinions expressed are however those of the authors only and do not necessarily reflect those of the European Union or the European Research Council. Neither the European Union nor the granting authority can be held responsible for them. We also thank the members of the International Space Science Institute (ISSI) International Team project #506 Understanding Mesoscale Ionospheric Electrodynamics Using Regional Data Assimilation for valuable insights and discussions related to this study. We extend out gratitude to the AMPERE team and the AMPERE Science Data Center for providing the field-aligned current data product derived from Iridium Communications constellation and providing the processed Iridium magnetic field measurements. For the ground magnetometer data we gratefully acknowledge: INTERMAGNET, Alan Thomson; CARISMA, PI Ian Mann; CANMOS, Geomagnetism Unit of the Geological Survey of Canada; The S-RAMP Database, PI K. Yumoto and Dr. K. Shiokawa; The SPIDR database; AARI, PI Oleg Troshichev; The MACCS program, PI M. Engebretson; GIMA; MEASURE, UCLA IGPP and Florida Institute of Technology; SAMBA, PI Eftyhia Zesta; 210 Chain, PI K. Yumoto; SAMNET, PI Farideh Honary; IMAGE, PI Liisa Juusola; Finnish Meteorological Institute, PI Liisa Juusola; Sodankylä Geophysical Observatory, PI Tero Raita; UiT the Arctic University of Norway, Tromsø Geophysical Observatory, PI Magnar G. Johnsen; GFZ German Research Centre For Geosciences, PI Jürgen Matzka; Institute of Geophysics, Polish Academy of Sciences, PI Anne Neska and Jan Reda; Polar Geophysical Institute, PI Alexander Yahnin and Yarolav Sakharov; Geological Survey of Sweden, PI Gerhard Schwarz; Swedish Institute of Space Physics, PI Masatoshi Yamauchi; AUTUMN, PI Martin Connors; DTU Space, Thom Edwards and PI Anna Willer; South Pole and McMurdo Magnetometer, PI's Louis J. Lanzarotti and Alan T. Weatherwax; ICESTAR; RAPIDMAG; British Artarctic Survey; McMac, PI Dr. Peter Chi; BGS, PI Dr. Susan Macmillan; Pushkov Institute of Terrestrial Magnetism, Ionosphere and Radio Wave Propagation (IZMIRAN); MFGI, PI B. Heilig; Institute of Geophysics, Polish Academy of Sciences, PI Anne Neska and Jan Reda; University of L'Aquila, PI M. Vellante; BCMT, V. Lesur and A. Chambodut; Data obtained in cooperation with Geoscience Australia, PI Andrew Lewis; AALPIP, co-PIs Bob Clauer and Michael Hartinger; MagStar, PI Valladares; SuperMAG, PI Jesper W. Gjerloev; Data obtained in cooperation with the Australian Bureau of Meteorology, PI Richard Marshall.

References

Aksnes, A., Stadsnes, J., Bjordal, J., Østgaard, N., Vondrak, R. R., Detrick, D. L., et al. (2002). Instantaneous ionospheric global conductance maps during an isolated substorm. *Annales Geophysicae*, *20*(8), 1181–1191. https://doi.org/10.5194/ANGEO-20-1181-2002

Amm, O. (1997). Ionospheric elementary current systems in spherical coordinates and their application. *Tech. Rep. No. 7*, *49*, 947–955. https://doi.org/10.5636/jgg.49.947

Amm, O., Engebretson, M. J., Hughes, T., Newitt, L., Viljanen, A., & Watermann, J. (2002). A traveling convection vortex event study: Instantaneous ionospheric equivalent currents, estimation of field-aligned currents, and the role of induced currents. *Journal of Geophysical Research*, *107*(A11), SIA1-1–SIA1-11. https://doi.org/10.1029/2002JA009472

Amm, O., & Viljanen, A. (1999). Ionospheric disturbance magnetic field continuation from the ground to the ionosphere using spherical elementary current systems. *Earth Planets and Space*, *51*(6), 431–440. https://doi.org/10.1186/BF03352247

Anderson, B. J., Angappan, R., Barik, A., Vines, S. K., Stanley, S., Bernasconi, P. N., et al. (2021). Iridium communications satellite constellation data for study of Earth's magnetic field. *Geochemistry, Geophysics, Geosystems*, *22*(8), e2020GC009515. https://doi.org/10.1029/2020GC009515

Anderson, B. J., Korth, H., Waters, C. L., Green, D. L., Merkin, V. G., Barnes, R. J., & Dyrud, L. P. (2014). Development of large-scale Birkeland currents determined from the active magnetosphere and planetary electrodynamics response experiment. *Geophysical Research Letters*, *41*(9), 3017–3025. https://doi.org/10.1002/2014GL059941

Anderson, B. J., Takahashi, K., Kamei, T., Waters, C. L., & Toth, B. A. (2002). Birkeland current system key parameters derived from Iridium observations: Method and initial validation results. *Journal of Geophysical Research*, *107*(A6), SMP11-1–SMP11-13. https://doi.org/10.1029/2001JA000080

Boström, R. (1964). A model of the auroral electrojets. *Journal of Geophysical Research*, *69*(23), 4983–4999. https://doi.org/10.1029/JZ069I023P04983

Coxon, J. C., Milan, S. E., & Anderson, B. J. (2018). A review of birkeland current research using AMPERE. In *Electric currents in geospace and beyond* (pp. 257–278). https://doi.org/10.1002/9781119324522.CH16

Dungey, J. W. (1963). In C. deWitt, J. Hieblot, & L. leBeau (Eds.), *Geophysics: The Earth's environment* (Vol. 503). Gordon and Breach.

Forsyth, C., Rae, I. J., Coxon, J. C., Freeman, M. P., Jackman, C. M., Gjerloev, J., & Fazakerley, A. N. (2015). A new technique for determining Substorm Onsets and Phases from Indices of the Electrojet (SOPHIE). *Journal of Geophysical Research: Space Physics*, *120*(12), 10592–10606. https://doi.org/10.1002/2015JA021343

Forsyth, C., Shortt, M., Coxon, J. C., Rae, I. J., Freeman, M. P., Kalmoni, N. M., et al. (2018). Seasonal and temporal variations of field-aligned currents and ground magnetic deflections during substorms. *Journal of Geophysical Research: Space Physics*, *123*(4), 2696–2713. https://doi.org/10.1002/2017JA025136

Frey, H. U., Østgaard, N., Immel, T. J., Korth, H., & Mende, S. B. (2004). Seasonal dependence of localized, high-latitude dayside aurora (HiLDA). *Journal of Geophysical Research*, *109*(A4), A04303. https://doi.org/10.1029/2003JA010293

Fukushima, N. (1976). Generalized theorem for no ground magnetic effect of vertical currents connected with Pedersen currents in the uniform-conductivity ionosphere. *Report of Ionosphere and Space Research in Japan*, *30*(1–2), 35–40.

Fukushima, N. (1994). Some topics and historical episodes in geomagnetism and aeronomy. *Journal of Geophysical Research*, *99*(A10), 19113–19142. https://doi.org/10.1029/94ja00102

Gjerloev, J. W. (2012). The SuperMAG data processing technique. *Journal of Geophysical Research*, *117*(9), A09213. https://doi.org/10.1029/2012JA017683

Gjerloev, J. W., & Hoffman, R. A. (2014). The large-scale current system during auroral substorms. *Journal of Geophysical Research: Space Physics*, *119*(6), 4591–4606. https://doi.org/10.1002/2013JA019176

Green, D. L., Waters, C. L., Korth, H., Anderson, B. J., Ridley, A. J., & Barnes, R. J. (2007). Technique: Large-scale ionospheric conductance estimated from combined satellite and ground-based electromagnetic data. *Journal of Geophysical Research*, *112*(5), A05303. https://doi.org/10.1029/2006JA012069

Harang, L. (1946). The mean field of disturbance of polar geomagnetic storms. *Journal of Geophysical Research*, *51*(3), 353–380. https://doi.org/10.1029/te051i003p00353

Juusola, L., Kauristie, K., Vanhamäki, H., Aikio, A., & van de Kamp, M. (2016). Comparison of auroral ionospheric and field-aligned currents derived from Swarm and ground magnetic field measurements. *Journal of Geophysical Research: Space Physics*, *121*(9), 9256–9283. https://doi.org/10.1002/2016JA022961

Kamide, Y., Richmond, A. D., & Matsushita, S. (1981). Estimation of ionospheric electric fields, ionospheric currents, and field-aligned currents from ground magnetic records. *Journal of Geophysical Research*, *86*(A2), 801–813. https://doi.org/10.1029/ja086ia02p00801

Kepko, L., McPherron, R. L., Amm, O., Apatenkov, S., Baumjohann, W., Birn, J., et al. (2015). Substorm current wedge revisited. *Space Science Reviews*, *190*(1–4), 1–46. https://doi.org/10.1007/S11214-014-0124-9/FIGURES/13

Laundal, K. M., Finlay, C. C., Olsen, N., & Reistad, J. P. (2018). Solar wind and seasonal influence on ionospheric currents from swarm and CHAMP measurements. *Journal of Geophysical Research: Space Physics*, *123*(5), 4402–4429. https://doi.org/10.1029/2018JA025387

Laundal, K. M., Gjerloev, J. W., Østgaard, N., Reistad, J. P., Haaland, S., Snekvik, K., et al. (2016). The impact of sunlight on high-latitude equivalent currents. *Journal of Geophysical Research: Space Physics*, *121*(3), 2715–2726. https://doi.org/10.1002/2015JA022236

Laundal, K. M., Reistad, J. P., Hatch, S. M., Madelaire, M., Walker, S. J., Hovland, A. Ø., et al. (2022). Local mapping of polar ionospheric electrodynamics. *Journal of Geophysical Research: Space Physics*, *127*(5), e2022JA030356. https://doi.org/10.1029/2022JA030356

Laundal, K. M., & Toresen, M. (2018). klaundal/pyAMPS: pyAMPS 0.1.0. https://doi.org/10.5281/ZENODO.1182931

Laundal, K. M., Yee, J.-H. H., Merkin, V. G., Gjerloev, J. W., Vanhamäki, H., Reistad, J. P., et al. (2021). Electrojet estimates from mesospheric magnetic field measurements. *Journal of Geophysical Research: Space Physics*, *126*(5), 1–17. https://doi.org/10.1029/2020ja028644

Liu, J., Angelopoulos, V., Chu, X., Zhou, X. Z., & Yue, C. (2015). Substorm current wedge composition by wedgelets. *Geophysical Research Letters*, *42*(6), 1669–1676. https://doi.org/10.1002/2015GL063289

Marklund, G., Sandahl, I., & Opgenoorth, H. (1982). A study of the dynamics of a discrete auroral arc. *Planetary and Space Science*, *30*(2), 179–197. https://doi.org/10.1016/0032-0633(82)90088-5

McPherron, R. L. (1970). Growth phase of magnetospheric substorms. *Journal of Geophysical Research*, *75*(28), 5592–5599. https://doi.org/10.1029/JA075i028p05592

McPherron, R. L., Russell, C. T., & Aubry, M. P. (1973). Satellite studies of magnetospheric substorms on August 15, 1968: 9. Phenomenological model for substorms. *Journal of Geophysical Research*, *78*(16), 3131–3149. https://doi.org/10.1029/JA078I016P03131

Milan, S. E., Clausen, L. B., Coxon, J. C., Carter, J. A., Walach, M. T., Laundal, K., et al. (2017). Overview of solar wind–magnetosphere–ionosphere–atmosphere coupling and the generation of magnetospheric currents. *Space Science Reviews*, *206*(1–4), 547–573. https://doi.org/10.1007/s11214-017-0333-0

Newell, P. T., & Gjerloev, J. W. (2011). Substorm and magnetosphere characteristic scales inferred from the SuperMAG auroral electrojet indices. *Journal of Geophysical Research*, *116*(12), A12232. https://doi.org/10.1029/2011JA016936

Nishimura, Y., Lyons, L. R., Gabrielse, C., Weygand, J. M., Donovan, E. F., & Angelopoulos, V. (2020). Relative contributions of large-scale and wedgelet currents in the substorm current wedge. *Earth Planets and Space*, *72*(1), 1–10. https://doi.org/10.1186/S40623-020-01234-X/FIGURES/6

Ohtani, S., & Gjerloev, J. W. (2020). Is the substorm current wedge an ensemble of wedgelets? Revisit to midlatitude positive bays. *Journal of Geophysical Research: Space Physics*, *125*(9), e2020JA027902. https://doi.org/10.1029/2020JA027902

Ronchi, C., Iacono, R., & Paolucci, P. S. (1996). The "cubed sphere": A new method for the solution of partial differential equations in spherical geometry. *Journal of Computational Physics*, *124*(1), 93–114. https://doi.org/10.1006/jcph.1996.0047

Sadourny, R. (1972). Conservative finite-difference approximations of the primitive equations on quasi-uniform spherical grids. *Monthly Weather Review*, *100*(2), 136–144. https://doi.org/10.1175/1520-0493(1972)100⟨0136:CFAOTP⟩2.3.CO;2

Schillings, A., Palin, L., Bower, G. E., Opgenoorth, H. J., Milan, S. E., Kauristie, K., et al. (2023). Signatures of wedgelets over Fennoscandia during the St Patrick's Day Storm 2015. *Journal of Space Weather and Space Climate*, *13*, 19. https://doi.org/10.1051/SWSC/2023018

Vanhamäki, H., & Juusola, L. (2020). Introduction to spherical elementary current systems. In *Ionospheric multi-spacecraft analysis tools* (pp. 5–33). Springer International Publishing. https://doi.org/10.1007/978-3-030-26732-2_2

Vasylinas, V. M. (2007). The mechanical advantage of the magnetosphere: Solar-wind-related forces in the magnetosphere-ionosphere-Earth system. *Annales Geophysicae*, *25*(1), 255–269. https://doi.org/10.5194/ANGEO-25-255-2007

Virtanen, P., Gommers, R., Oliphant, T. E., Haberland, M., Reddy, T., Cournapeau, D., et al. (2020). SciPy 1.0: Fundamental algorithms for scientific computing in Python. *Nature Methods 2020*, *17*(3), 261–272. https://doi.org/10.1038/s41592-019-0686-2

Walker, S. (2023). The ionospheric leg of the substorm current wedge: Combining iridium and ground magnetometers [Dataset]. *Zenodo*. https://doi.org/10.5281/zenodo.13933677

Walker, S., Laundal, K., Reistad, J., Ohma, A., & Hatch, S. (2023). Statistical temporal variations in the auroral electrojet estimated with ground magnetometers in Fennoscandia. *Space Weather*, *21*(1), e2022SW003305. https://doi.org/10.1029/2022SW003305

Waters, C. L., Anderson, B. J., Green, D. L., Korth, H., Barnes, R. J., & Vanhamäki, H. (2020). Science data products for AMPERE. *Ionospheric Multi-Spacecraft Analysis Tools*, 141–165. https://doi.org/10.1007/978-3-030-26732-2_7

Waters, C. L., Anderson, B. J., & Liou, K. (2001). Estimation of global field aligned currents using the iridium® System magnetometer data. *Geophysical Research Letters*, *28*(11), 2165–2168. https://doi.org/10.1029/2000GL012725

Weygand, J. M., Engebretson, M. J., Pilipenko, V. A., Steinmetz, E. S., Moldwin, M. B., Connors, M. G., et al. (2021). SECS analysis of nighttime magnetic perturbation events observed in Arctic Canada. *Journal of Geophysical Research: Space Physics*, *126*(11), e2021JA029839. https://doi.org/10.1029/2021JA029839

Weygand, J. M., & Wing, S. (2016). Comparison of DMSP and SECS region-1 and region-2 ionospheric current boundary. *Journal of Atmospheric and Solar-Terrestrial Physics*, *143–144*, 8–13. https://doi.org/10.1016/j.jastp.2016.03.002